Body-wave extraction and tomography at Long Beach, CA, with ambient-noise interferometry

Nori Nakata, Jason P. Chang, and Jesse F. Lawrence

ABSTRACT

We retrieve diving P waves by applying seismic interferometry to ambient noise records observed at Long Beach, California, and invert travel times of these waves to estimate 3D P-wave velocity structure. The ambient noise is recorded by a dense and large network, which has about 2500 receivers with 100 m average spacing. In contrast to surface-wave extraction, body-wave extraction is much harder because body-wave energy is generally much weaker than surface waves in the regional scale (maximum offset is $\sim$ 10 km). For travel-time tomography, we need to extract body waves at each pair of receivers separately. Therefore, we employ two post-correlation filters to reject noisy signals (which are unusable for body-wave tomography). The first filter rejects traces based on low P-wave correlation with the stack of all traces at that distance. The second filter measures coherent energy between all retained traces and suppresses incoherent noise in each trace. With these filters, we can reconstruct clear body waves from each virtual source. Then we estimate 3D P-wave velocities from these waves with travel-time tomography. The velocities show high-resolution structure.

INTRODUCTION

Seismic interferometry, a type of cross-correlation analysis, is a powerful tool for extracting earth response from passive data at the local and global scales (e.g., Curtis et al., 2006; Ruigrok et al., 2010; Nishida, 2013). Theoretically, we can extract Green's functions by using seismic interferometry (Lobkis and Weaver, 2001; Snieder, 2004; Wapenaar and Fokkema, 2006), and this technique works well to reveal velocity and attenuation structures (e.g., Lin et al., 2009; Lawrence and Prieto, 2011). Although surface waves are easier to retrieve because of their strong energy in ambient noise (e.g., Campillo and Paul, 2003; Shapiro et al., 2005), some studies have found body waves (e.g., Roux et al., 2005; Poli et al., 2012). Draganov et al. (2009) and Nakata et al. (2011) used the extracted body waves for imaging with migration techniques.

Dense arrays are suitable for ambient-noise tomography, and Mordret et al. (2013) and de Ridder and Biondi (2013) discovered velocity structures in a regional (reservoir) scale using Scholte waves (interface waves between fluid and solid). At regional scales, body waves extracted by seismic interferometry are not clear enough for tomography. Therefore, in this study, we propose a technique to retrieve body waves

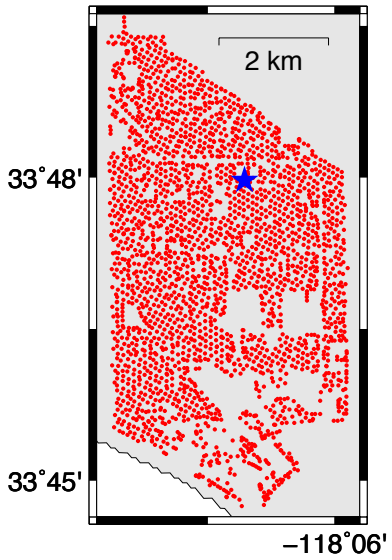

Figure 1: Map of receivers. The red dots show the location of receivers, and the blue star indicates the reference receiver used in Figure 2a. [**CR**]

from ambient noise data recorded at Long Beach, California, USA. Here, we first introduce the data set and initial virtual shot gathers. Then we present a technique to extract body waves. Finally, we show inverted velocity structures using travel-time tomography.

AMBIENT-NOISE DATASET AND SEISMIC INTERFEROMETRY

Ambient-noise data were acquired by NodalSeismic from January 2012 at Long Beach and continuously recorded for about three months. The array is uniquely dense (100 m spacing) and large (2500 receivers) compared with other arrays to record ambient noise. The receivers had only a vertical component, and our target is P waves propagating between each receiver pair. Figure 1 shows receiver locations. The receivers are fairly evenly distributed over an area of 8×4.5 km^2, though some small spots have no receivers. Using an adjacent array at Long Beach, Lin et al. (2013) revealed 3D shear-wave velocities from surface-wave ambient-noise tomography, and Schmandt and Clayton (2013) found crustal structure from teleseismic waves.

In this study, we use 10 days of data recorded by all receivers. These ambient noise data were resampled to 0.03 s sampling time, and we focus on body waves up to 15 Hz. To apply seismic interferometry, we compute power-normalized crosscorrelation between receivers A and B in the frequency domain given by

$$C(B,A,\omega) = \sum_t \frac{u_t(B,\omega)u_t^*(A,\omega)}{|u_t(B,\omega)||u_t^*(A,\omega)| + \epsilon}, \tag{1}$$

where $u_t(A,\omega)$ is an ambient-noise record observed at receiver A at time interval t,

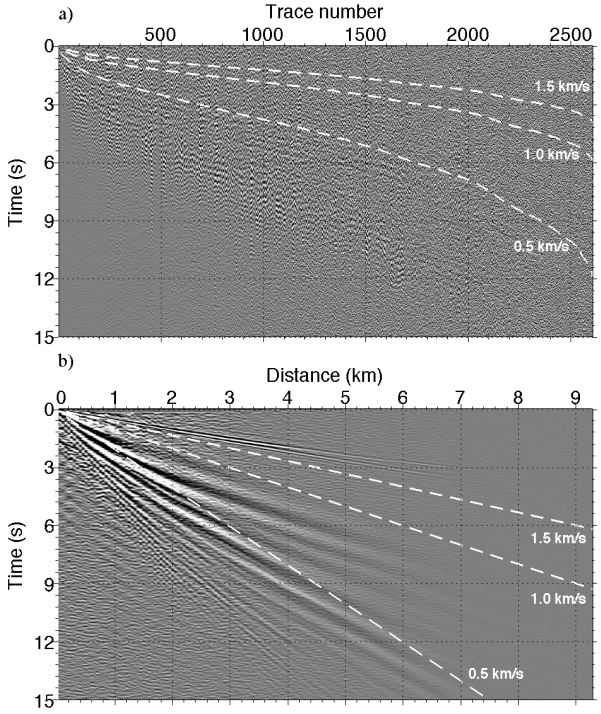

Figure 2: (a) Example of virtual shot gathers constructed from 10-day ambient-noise data. The virtual source is the blue star shown in Figure 1. Trace number is aligned with the distance from the virtual source. The frequency range is from 0.5 to 15.0 Hz. The blue lines indicate constant velocity travel times with an assumption of straight paths. (b) Stacked crosscorrelation gather over all virtual shot gathers. The bin for this spatial stacking is 50 m. The frequency range is the same as panel (a). The blue lines indicate constant velocity travel times with an assumption of straight paths. [**CR**]

which is one day here, in the frequency domain (ω), ϵ a regularization parameter (Nakata et al., 2013), and $*$ a complex conjugate. Expression 1 is a receiver-by-receiver process, and we create daily correlation by using this expression. When we use a sufficient amount of data, $C(B, A)$ represents wave propagation from receivers A to B, which means A becomes a virtual source. Because this formula does not specify wave types, we can apply expression 1 to surface and/or body waves. Figure 2a shows an example of a gather of $C(B, A)$, in which A is one receiver (the blue star in Figure 1) and B all receivers. To plot the gather, we average correlation over 10 days, and align traces only by offset between the virtual source and each receiver (ignoring azimuth). In Figure 2a, although we can reconstruct strong surface waves with apparent wave speeds between 0.4–0.9 km/s, we cannot find clear coherent signals faster than 1.5 km/s.

The reason why only surface waves are extracted/visible in Figure 2a is that surface-wave energy dominates the observed ambient-noise data with any body waves buried in the noise. In Figure 2b, we use all virtual-source gathers to detect the presence of body waves. We stack correlated waveforms over all daily correlations in each 50-m distance bin from each virtual source. The number of daily correlations in each bin is shown in the gray line in Figure 3, which indicates that we stack over a tremendous number of daily correlations to construct one trace in Figure 2b. Note that we use only 10 daily correlations to plot each trace in Figure 2a. In Figure 2b, we extract body waves, which are faster than 1.5 km/s. Because the wave starts propagating from around time zero and the apparent velocity of the

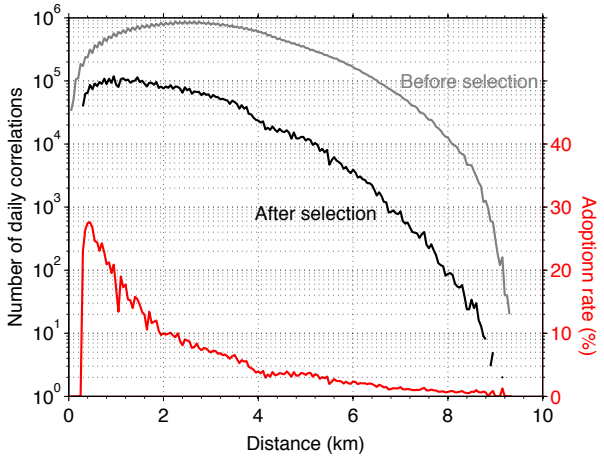

Figure 3: Number of traces before (gray) and after (black) the selection based on correlation coefficients at each bin. The red liner (right axis) illustrates adoption rate of traces. [**CR**]

wave increases in far offset, we assume this reconstructed wave is a diving P wave. Although this discovery of body waves is interesting, we cannot yet directly use the waves for tomography studies to estimate 3D velocity structure. Next, we use stacked correlations as a reference to retrieve body waves in each pair of receivers.

POST CORRELATION TECHNIQUES TO RETRIEVE BODY WAVES

We employ two steps to clean up the crosscorrelation functions. First, we select daily correlations which include stronger body-wave energy. After computing expression 1 and obtaining daily correlations, we can roughly assume the arrival time of diving P waves. To isolate body waves, we apply a time window with Gaussian-shape taper in each daily correlation to mute signals slower than 1.1 km/s and faster than 6.0 km/s. Then we compute a correlation coefficient between each trace in the daily correlation and a corresponding trace in a bin of the appropriate distance in Figure 2b. When the coefficient is smaller than 0.3, we discard the trace of the daily correlation. With this procedure, we retain about 10% of traces, which include stronger body waves (Figure 3). Figure 4a shows daily correlations before selection in the 3 km bin. By stacking traces over the horizontal axis in Figure 4a, we will obtain body waves as shown in Figure 2b, but we cannot find clear body-wave signals in each single trace. After selection, we reveal body waves with velocity around 2.0 km/s. Although this selection might be enough to find body waves, for tomography purposes, we further improve the quality of body waves.

The second step is applying an adaptive covariance filter (ACF), which is designed for ambient-noise analysis (Lawrence, 2014). We assume signals are coherent over all retained traces, and noise is incoherent in frequency or time. Therefore, we need results from the first step to make body waves coherent among traces. The ACF measures the coherent energy between all trace pairs in a data set and suppresses incoherent power in each trace. The filter uses $N(N-1)/2$ relative comparison rather

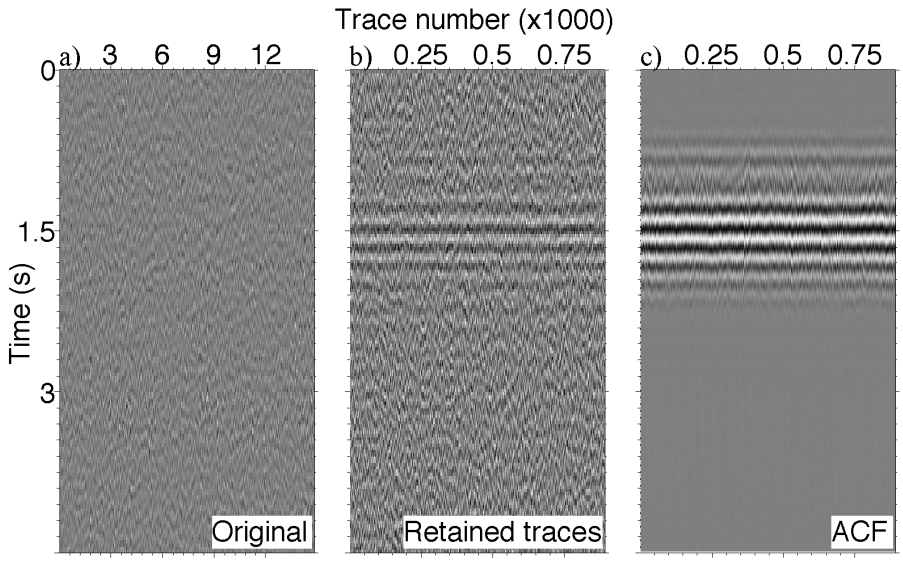

Figure 4: (a) Unfiltered traces in a bin at 3 km using all virtual sources. Each trace corresponds to each receiver pair reconstructed from one-day data. (b) Traces selected based on a correlation coefficients around body-wave time windows. (c) Traces after applying adaptive-covariance filter (ACF). Note that the number of traces in panels (b) and (c) are identical. We show only 2% of total number of traces in the bin. [**CR**]

than N observations, which yields results with higher signal-to-noise ratio (S/N). We apply this filter to traces in each bin to improve S/N (Figure 4c). From unfiltered correlation waveforms (Figure 4a), we clearly improve the quality of retrieved body waves, and our two steps allow us to estimate accurate travel times of the body waves at each trace. After applying ACF, we distribute filtered traces to each virtual source.

In Figure 5a, we show a virtual shot gather after the two steps. Note that each trace shows body-wave propagation between each pair of receivers. The diving wave propagates with a velocity around 2.0 km/s, and, as we expect, the apparent velocity increases with distance from the virtual source. Figure 5b illustrates time slices of wave propagation in Figure 5a. Selected receivers (large circles in Figure 5b) are almost evenly distributed all over the array; hence body waves in the ambient noise come from a wide range of angles. Also, body waves have no obvious directionality of velocities. Because we use amplitude-normalized crosscorrelation (equation 1) and ACF, relative amplitudes of body waves in Figure 5 may not be the same as the azimuthal strength of observed body waves. In some snapshots, clear wavefronts are reconstructed (e.g., 1.35 and 1.50 s). In the next section, we pick travel times of body waves at each pair of receivers from each virtual shot (Figure 5a) and estimate P-wave velocity structure with travel-time tomography.

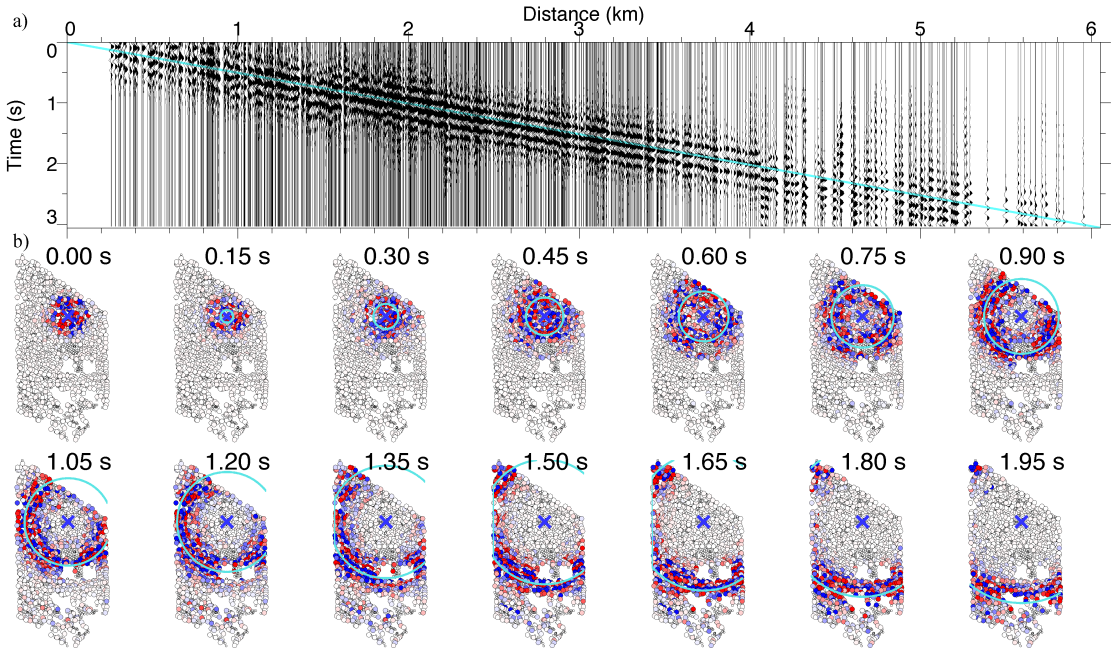

Figure 5: (a) Example of virtual-shot gathers of selected traces after the ACF is applied. The virtual source is shown in the blue star in Figure 1, and the blue line indicates the arrival time of the wave with velocity of 2.0 km/s. The horizontal axis is the distance from the virtual source. The frequency range is from 3.0 to 15.0 Hz. (b) Snapshots of body waves shown in panel (a). Each circle illustrates the location of receivers, and the blue circle shows a virtual source. At each receiver, blue is positive amplitude and red negative. The light blue line draws the traveling distance of the wave with velocity of 2.0 km/s. [**CR**]

BODY-WAVE TOMOGRAPHY

We implement body-wave tomography based on Hole (1992), assuming diving body waves. Figure 6 shows preliminary results of vertical and horizontal slices of the inverted 3D P-wave velocity structure. We invert the data with several 1D starting models and update the initial models during inversion. The inversion converges when travel-time misfits are sufficiently small. We show the final velocity structure in Figure 6. Figures 6a–c show P velocities anomalies relative to the best-fit 1D velocity (Figure 6d). According to ray tracing, diving waves reach up to 1.2-km depth. Note that the largest offset we can find body waves is 9.2 km, which is about the size of the array (Figure 1).

By using body waves, we obtain higher resolution velocity structure compared with similar surface-wave tomography (Lin et al., 2013). We must carefully scrutinize these preliminary results with a resolution and uncertainty test, but a higher velocity zone at the south part in Figure 6a may be related to the Newport-Inglewood fault.

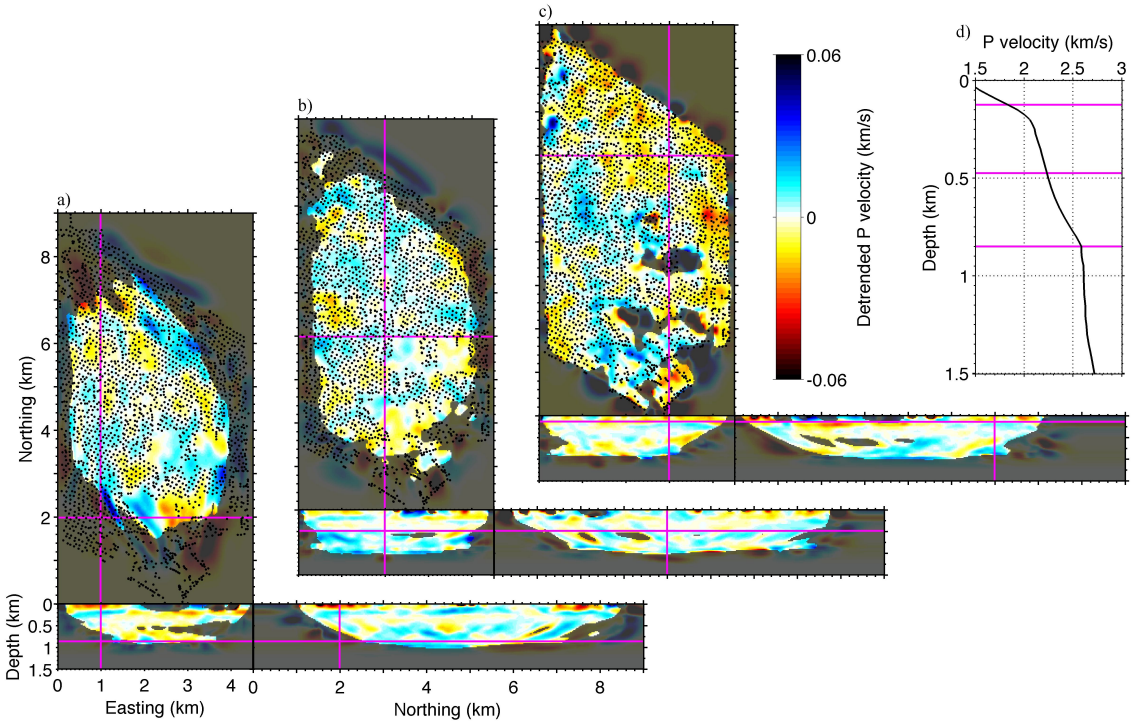

Figure 6: Vertical and horizontal slices of inverted P-wave velocity cube. From (a)–(c), slices shift shallower, east, and north. Purple lines show the location of slices. Velocities are detrended by subtracting the horizontally averaged one-dimensional velocities shown in panel (d). The colormap is valid for panels (a)-(c), where blue indicates faster velocities than the velocity in panel (d). The shaded areas in the velocity slices are poor ray coverage areas. The origin of local coordinate in this figure (Easting = 0 km and Northing = 0 km) is the lower-left corner in Figure 1. [**CR**]

CONCLUSIONS

We have successfully retrieved body waves that propagate between single pairs of receivers from a regional-scale dense array. To extract body waves, we use two steps of signal processing: selection of traces based on a correlation coefficient and the adaptive covariance filter. With this approach, each trace in virtual-shot gathers clearly shows diving P waves, and, using these waves, we estimate P-wave velocities. Because of the dense network, rays cover the entire area well, and we can invert high-resolution 3D velocity structures. This is one type of target-oriented seismic interferometry and is useful for estimating high-resolution velocity structure and imaging.

The maximum depth of ray coverage of this tomography is about 1.2 km. With larger-offset data, we could investigate deeper areas as like active-source tomography. In this study, we use only 10 days of data. One of the strong points for using passive data is in time-lapse survey, and by using this technique, we can potentially monitor

a region/reservoir at, for example, 10 day intervals.

ACKNOWLEDGEMENTS

We are grateful to Signal Hill Petroleum, Inc. for access to this dataset and permission to publish. We also thank Dan Hollis at NodalSeismic and John A. Hole at Virginia Tech for their professional help and comments.

REFERENCES

Campillo, M. and A. Paul, 2003, Long-range correlations in the diffuse seismic coda: Science, **299**, 547–549.

Curtis, A., P. Gerstoft, H. Sato, R. Snieder, and K. Wapenaar, 2006, Seismic interferometry - turning noise into signal: The Leading Edge, **25**, 1082–1092.

de Ridder, S. A. L. and B. L. Biondi, 2013, Daily reservoir-scale subsurface monitoring using ambient seismic noise: Geophys. Res. Lett., **40**, 2969–2974.

Draganov, D., X. Campman, J. Thorbecke, A. Verdel, and K. Wapenaar, 2009, Reflection images from ambient seismic noise: Geophysics, **74**, A63–A67.

Hole, J. A., 1992, Nonlinear high-resolution three-dimensional seismic travel time tomography: J. Geophys. Res., **97**, 6553–6562.

Lawrence, J. F., 2014, Improved seismic ambient noise analyses with the adaptive covariance filter: J. Geophys. Res.(in review).

Lawrence, J. F. and G. A. Prieto, 2011, Attenuation tomography of the western United States from ambient seismic noise: J. Geophys. Res., **116**, B06302.

Lin, F.-C., D. Li, R. W. Clayton, and D. Hollis, 2013, High-resolution 3D shallow crustal structure in Long Beach, California: Application of ambient noise tomography on a dense seismic array: Geophysics, **78**, Q45–Q56.

Lin, F.-C., M. H. Ritzwoller, and R. Snieder, 2009, Eikonal tomography: surface wave tomography by phase front tracking across a regional broad-band seismic array: Geophys. J. Int., **177**, 1091–1110.

Lobkis, O. I. and R. L. Weaver, 2001, On the emergence of the Green's function in the correlations of a diffuse field: J. Acoust. Soc. Am., **110**, 3011–3017.

Mordret, A., M. Landès, N. M. S. C. Singh, P. Roux, and O. I. Barkved, 2013, Near-surface study at the Valhall oil field from ambient noise surface wave tomography: Geophys. J. Int., **193**, 1627–1643.

Nakata, N., R. Snieder, S. Kuroda, S. Ito, T. Aizawa, and T. Kunimi, 2013, Monitoring a building using deconvolution interferometry. I: Earthquake-data analysis: Bull. Seismol. Soc. Am., **103**, 1662–1678.

Nakata, N., R. Snieder, T. Tsuji, K. Larner, and T. Matsuoka, 2011, Shear-wave imaging from traffic noise using seismic interferometry by cross-coherence: Geophysics, **76**, SA97–SA106.

Nishida, K., 2013, Global propagation of body waves revealed by cross-correlation analysis of seismic hum: Geophys. Res. Lett., **40**, 1691–1696.

Poli, P., M. Campillo, H. Pedersen, and L. W. Group, 2012, Body-wave imaging of Earth's mantle discontinuities from ambient seismic noise: Science, **338**, 1063–1065.

Roux, P., K. Sabra, P. Gerstoft, and W. Kuperman, 2005, P-waves from cross correlation of seismic noise: Geophys. Res. Lett., **32**, L19303.

Ruigrok, E., X. Campman, D. Draganov, and K. Wapenaar, 2010, High-resolution lithospheric imaging with seismic interferometry: Geophys. J. Int., **183**, 339–357.

Schmandt, B. and R. W. Clayton, 2013, Analysis of teleseismeic P waves with a 5200-station array in Long Beach, California: Evidence of an abrupt boundary to Inner Borderland rifting: J. Geophys. Res., **118**, 5320–5338.

Shapiro, N. M., M. Campillo, L. Stehly, and M. H. Ritzwoller, 2005, High-resolution surface-wave tomography from ambient seismic noise: Science, **307**, 1615–1618.

Snieder, R., 2004, Extracting the Green's function from the correlation of coda waves: A derivation based on stationary phase: Phys. Rev. E, **69**, 046610.

Wapenaar, K. and J. Fokkema, 2006, Green's function representations for seismic interferometry: Geophysics, **71**, SI33–SI46.